PAPER

Check for updates

Lubricating properties of single metal ions at interfaces†

Clodomiro Cafolla (iD) and Kislon Voïtchovsky (iD) *

The behaviour of ionic solutions confined in nanoscale gaps is central to countless processes, from bio-molecular function to electrochemistry, energy storage and lubrication. However, no clear link exists between the molecular-level behaviour of the liquid and macroscopic observations. The problem mainly comes from the difficulty to interrogate a small number of liquid molecules. Here, we use atomic force microscopy to investigate the viscoelastic behaviour of pure water and ionic solutions down to the single ion level. The results show a glassy-like behaviour for pure water, with single metal ions acting as lubri-cants by reducing the elasticity of the nano-confined solution and the magnitude of the hydrodynamic friction. At small ionic concentration (<20 mM) the results can be quantitatively explained by the ions moving *via* a thermally-activated process resisted by the ion's hydration water (Prandtl–Tomlinson model). The model breaks down at higher salt concentrations due to ion-ion interaction effects that can no longer be neglected. The correlations are confirmed by direct sub-nanometre imaging of the interface at equilibrium. The results provide a molecular-level basis for explaining the tribological properties of aqueous solutions and suggest that ion-ion interactions create mesoscale effects that prevent a direct link between nanoscale and macroscopic measurements.

Introduction

Interfaces between solids and aqueous solutions are ubiqui-tous in nature,[1] often confined to nano-gaps, inside or between solids.[2] Examples range from biomolecules folding[3] and microcirculation of metabolites in cells[4] to the growth of minerals[5] and geochemistry.[6] In technology, the role played by this so-called nano-confined[7] water is arguably even more central with applications in electrochemistry and energy science,[8] colloidal science,[9] biomedical sciences,[10] hetero-geneous catalysis,[11] tribology and lubrication.[12] Nano-confined water does not, generally, behave like its bulk counterpart; water molecules tend to be more ordered due to their inter-actions with the surface[2,13] and reduced conformational entropy.[14] This molecular ordering vanishes over a few mole-cular diameters (typically < 1–2 nm) in the bulk liquid,[15] but the specific organisation and dynamics of the interfacial water molecules depend on the details of each system.[2,15–17] Parameters such as the chemical nature and the geometry of the confining surfaces,[8,15] as well as the presence of dissolved molecules and ions,[18] can dramatically influence the behav-iour of interfacial water.[19] The importance of interfacial effects

is further emphasised for nano-confined water in systems where every liquid molecule can be seen as belonging to one or more interfaces. Additionally, the pressure and the tempera-ture within the nano-confined gap,[19–21] as well as a possible relative motion of the confining surfaces,[22] can influence both the molecular arrangement and the dynamics of the nano-confined solution.

Numerous studies[2,6,7,12–15,17,20–37] have examined the behaviour of nano-confined aqueous solutions in various systems and under different circumstances. Experimentally, the two main approaches are based on the surface force appar-atus (SFA) and atomic force microscopy (AFM) with each family of methods offering different modes of operation. The SFA-related methods rely on a well-defined confinement geo-metry between atomically flat surfaces over a large area (typi-cally several μm²).[22,28,31,33,38–41] The distance between the con-fining surfaces can be measured in an absolute manner using interferometry, and dynamical measurements of the visco-elastic properties of confined aqueous solutions are possible over a range of frequencies (typically 1–3 Hz) using surface force balances (SFB),[42] or SFA with resonance detec-tion.[33,38,40,41] In contrast, AFM-based methods probe a small number of liquid molecules, typically located between a nano-metre sharp tip and an atomically surface.[2,43,44] The exact con-finement geometry is less well controlled, unless the tip radius is artificially increased.[45] This is both a drawback and an advantage over SFA-based methods. On the one hand, AFM is

Physics Department, Durham University, Durham DH1 3LE, UK.
E-mail: kislon.voitchovsky@durham.ac.uk

able to probe systems locally, with minimal area averaging, and with sub-nanometre precision in all directions.[24,44] AFM allows for molecular-level imaging of the confined liquid,[44,46] direct identification of possible contaminant,[47] and avoids mesoscale averaging effects. On the other hand, the small confinement area and poor control of the tip geometry can render interpretation of results challenging, especially in the absence of an absolute measurement of the confining gap's thickness.

Recently, both techniques have been used to investigate the effects of dissolved metal ions on the behaviour of nano-confined water.[31,32,39,42,48–50] SFB studies indicate that ultrapure water remains mostly fluid even when confined to gaps <3.5 nm, resulting in a 3–5 fold increase in viscosity.[22,28,42,49] This result is supported by some theoretical studies,[51,52] and explained by a fast rotational and translational dynamics of water molecules under extreme confinement.[51] In contrast, AFM measurements suggest anomalous behaviour of nanoconfined water, with an effective viscosity that increases by orders of magnitude for nanoscale gaps between hydrophilic surfaces.[17,29] This is also supported by some theoretical studies: Monte Carlo simulations showed that water molecules in contact with mica's ditrigonal cavities exhibit a residence time almost 10 times greater than that of bulk water.[30]

Dissolving metal salts into the water does not reconcile the techniques. SFB studies show a general tendency for metal ions to increase the lubrication of water films confined between negatively charged mica surfaces, at least for ionic concentrations in the order of 100 mM NaCl.[39,42,49] This was interpreted as due to the shear rate being smaller than the hydration shell relaxation rate:[50] rapid exchange of water molecules between ions and the mica (in the order of 10^9 s^{-1}) ensures that the surface-bound hydration layer remains fluid at the shear rates (up to 10^3 s^{-1}).[48] Different ions give rise to a wide range of lubricating properties, usually more effective for ions with a higher charge density[39,42] suggesting a more robust Stern layer. In contrast, AFM experiments on various concentrations of NaCl suggest the confined ions act as pinning centres for water molecules, restricting their mobility and increasing the effective elasticity of the system.[32]

The discrepancies between techniques highlight gaps in our understanding of the behaviour of nano-confined aqueous solutions. The confining constraints and the spatial scale of observations are just but two potential factors responsible for the divergent findings, in particular when taking into account the observed molecular arrangement of the sheared liquid film.[33] Ions do not necessarily arrange randomly at the surface of solids, but instead can form organised nanoscale clusters through water-mediated correlations,[24] and with millisecond dynamics at the single ion level.[23,53] While only a handful of reports evidence mesoscale order (1–100 nm),[24,25] its origin would suggest mesoscale effects to be the rule rather than the exception. In nano-shearing experiments, mesoscale order could have significant consequences for the dynamics and lubrication properties of the system depending on the scale considered.[23–25,54] Molecular-level measurements also need to

address boundary effets[55] and any surface singularities that prevent mean field simplifications.

The present study investigates the tribological properties of aqueous solutions confined between an AFM tip and a flat mica surface at the single ion level. We explore the impact of charge density and pH on the viscoelastic response of the nano-confined liquid. The results provide quantitative insights into the lubrication properties of nano-confined solution, including the conditions leading to the breakdown of the simple molecular-level descriptions that neglect system-specific effects.

Experimental

Sample preparation

High-quality V1 muscovite mica disc (SPI Supplies, West Chester, PA, USA) glued to a steel plate was freshly cleaved and rinsed copiously with ultra-pure water (Water AnalaR NORMAPUR, VWR International Ltd, Leicestershire, UK). All the solutions were prepared in ultrapure water with 99.9% pure salts (Sigma-Aldrich, St Louis, MO, USA). pH adjustment was done with a solution of fuming 37% hydrochloric acid (HCl, Merck Millipore, Billerica, MA, USA). No buffering agent was used to avoid interfering with the measurements.[56,57] Testing of the pH was also conducted immediately after conducting experiments to ensure stability.

Atomic force microscopy measurements

The measurements were performed using a commercial Cypher ES AFM system (Oxford Instruments, Santa Barbara, CA, USA), equipped with temperature control. All the experiments were conducted with silicon nitride cantilevers originating from a same wafer (Olympus RC800 PSA, Olympus, Tokyo, Japan) with a nominal flexural spring constant, $k_f = 0.39$ N m^{-1}. Each cantilever was calibrated using its thermal spectrum[58] yielding a typical stiffness of 0.33 (±0.05) N m^{-1} in solution. Calibration of the torsional cantilever inverse optical lever sensitivity (InvOLS) and spring constant, k_t, is a more demanding procedure[59] and was hence performed only on 5 cantilevers. We found $k_t = 184$ (±1) N m^{-1}. The calibration procedure is described, in detail, in ESI.†

At least, three full sets of measurement (>100 curves each) were obtained in any given solution. For a given series, measurements were first conducted in ultrapure water, followed by monovalent, and then divalent salts. The monovalent ion solutions were tested in no particular order between the different sets in order to minimize the risk of systematic errors. When exchanging solutions within a given series, the tip was thoroughly washed with pure water (20 times with 100 μl) and then with the new solution of interest (40 times with 100 μl). This ensured that only the metal ions of interest were present on the mica surface (see also ESI†). Particular attention was paid to avoid any possible sources of contamination (cleaning procedures detailed in ESI†).[47]

Imaging of the confined Stern layer and hydration landscape was conducted with sub-nanometre resolution. The AFM

was operated in amplitude-modulation using photothermal excitation. The ratio A/A_0, between the imaging amplitude and the free amplitude (away from the surface) was kept as high as possible,[24] with A between 0.8–1.5 nm. When operating in this regime, atomic level resolution of the interface could be routinely achieved.[25,47,60]

Shear-force spectroscopy

The shearing measurements were acquired over typically five different locations in each solution (at least three) resulting in ~100 shear-force curves that were subsequently averaged. The AFM effectively functions as a nanoscopic linear rheometer (1.1 kHz), with sub-nanometre lateral oscillation amplitudes of ~0.5 nm chosen to equate the distance between two adjacent lattice sites for adsorbed ions.[61,62] Standard force–distance curves are then acquired recording simultaneously three quantities: (i) the normal defection of the cantilever, directly related to the confining force/pressure, (ii) the measured shear amplitude, A_t, and (iii) the phase lag, φ_t, between the driving shear and the resulting tip motion (see ESI, Fig. S1,† for a representative example).[63] The shear amplitude A_t is always taken as peak to peak throughout this study, and the approaching speed of the tip towards the surface set to 10 nm s^{-1}. For small torsional amplitudes, the magnitude of the time-averaged shear-force, F_{shear}, can be directly calculated from A_t:

$$F_{shear} = A_t k_t, \qquad (1)$$

where k_t is the torsional spring constant of the cantilever. When $\varphi_t = 0°$, the cantilever torsion is in phase with the lateral oscillation of the sample and the coupling is perfectly elastic.

In contrast, if $\varphi_t = 90°$, the coupling is perfectly viscous. The average energy dissipated per shear cycle, E_{diss}, can be calculated from the viscous part of the work carried out by the tip over an oscillation cycle:

$$E_{diss} = 2A_t F_{shear} \sin(\varphi_t). \qquad (2)$$

It should be noted that eqn (2) relies on averaged quantities since the instantaneous (oscillating) shear forces and phases are not accessible with our setup. As such, the energy dissipated over a cycle is simply modelled as the product of the viscous component of the shear force and the total distance, $2A_t$, travelled by the tip over a full shear cycle.

Accurate derivation of F_{shear} and E_{diss} hinges on a careful calibration of the system and the tip moving perfectly in phase with the driving signal. The system calibration is described, in detail, in ESI,† including control experiments with the tip pinned to the sample (perfectly elastic shear) to confirm that no additional phase lag, induced by possible delays in the mechanical motion of the oscillating scanner, occurs (see ESI, Fig. S2 and S3†).

Since A_t, φ_t, and hence F_{shear} and E_{diss} depend on the applied confining force, it is useful to present them as functions of the later. In this study, we consistently present F_{shear}, φ_t and E_{diss} as functions of the confining force. We note that if the confinement area is known (typically ~10 nm^2),

F_{shear} and E_{diss} can also be expressed as functions of the confining pressure. Here, the confining pressure increases by ~100 MPa for every nanonewton load (nN) applied.

Controlling the confinement is difficult with AFM, and tip asperities can significantly affect the reproducibility of shear force measurements. To address this issue and remove unreproducible tip asperities, each tip was gently 'blunted' in a controlled manner at the beginning of the experiments. This resulted in typical tip radii of 15–20 nm (see ESI, Fig. S4†). The quality of the images (Fig. 1) collected with 'blunted' tips confirms the tips are still sharp enough for high-resolution imaging.

Analysis and calculations derived from the shear data was performed using homemade routines programmed in Igor Pro (Wavemetrics, Lake Oswego, OR, USA) and Python.

Results and discussion

High-resolution imaging of the confined interface

Fig. 1 presents some high-resolution images of the mica surface in the different solutions. In all cases, atomic-level details are visible, but the quality of the image and the existence of mesoscale order depends on each imaging solution. The mesoscale patterns for the different ions are reproducible over multiple independent experiments. In pure water, the pseudo-hexagonal crystal structure appears clearly both in the topography and phase images. Water molecules form well-ordered hydration layers that extend up to 1 nm in the bulk solution[62] and follow the mica lattice arrangements. Adsorbed K^+ and Rb^+ ions tend to form small domains due to water-mediated attractive lateral interactions when at the interface,[23,24] inducing near-uniform looking layer in 5 mM RbCl[24] and ordered longitudinal domains in KCl at the same concentration. This is consistent with the hydration structures of Rb^+ and K^+ ions, with both ions adsorbing mainly in a single hydration state to the mica substrate. In contrast, Na^+ ions can adopt different hydration states (inner and outer shell coordination),[64] rendering the AFM images less uniform (Fig. 1d). Marked localised height variations are visible resulting in noisier images due to the higher mobility of adsorbed Na^+ ions. Divalent Ca^{2+} ions can also adopt multiple hydration states and adsorb at both the centre of the ditrigonal cavities (position 1 the cartoon in Fig. 1f) and at interstitial sites[64] (position 2 in Fig. 1f). Domains similar to those induced by K^+ are visible, but Ca^{2+} ions are bound more strongly to the mica and cannot be easily removed.[64]

Shear-spectroscopy: hard confinement

The high-resolution images shown in Fig. 1 highlight the importance of local hydration effects on the organisation and the behaviour of the different ions at the interface. Order can exist both at the molecular (single-ion) level and at the mesoscale, inducing variations in the hydration landscape of the interface. To single out the impact of single ions on the lubrication of the interface, we conducted shear-force spectroscopy
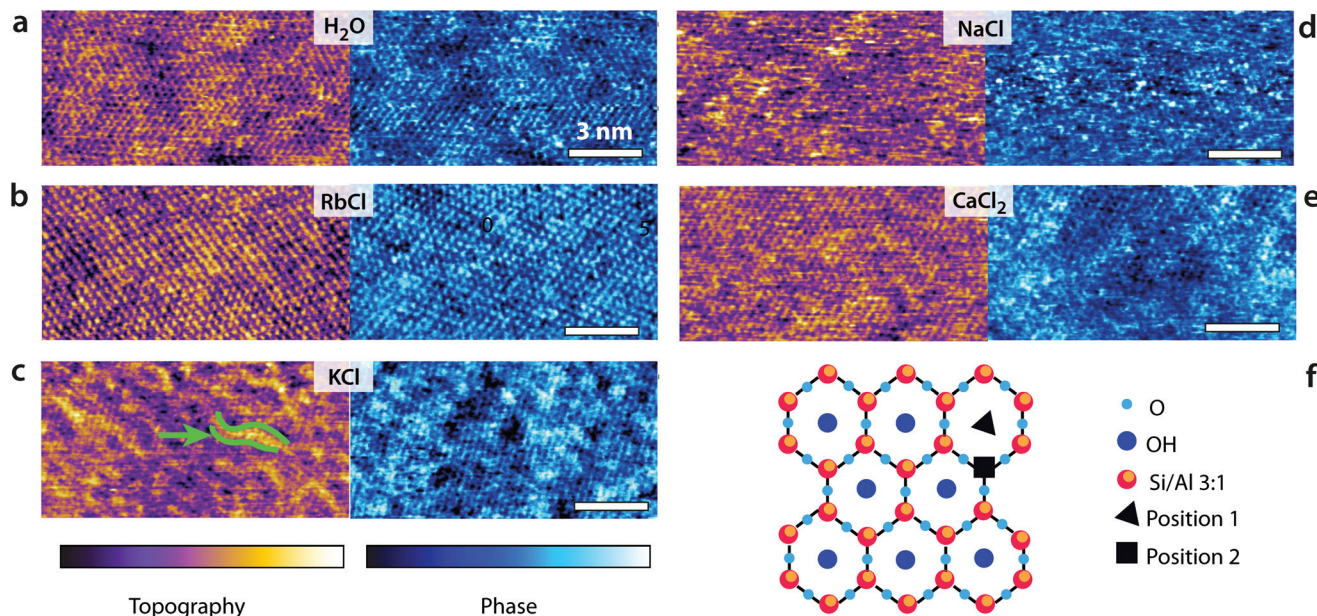
Fig. 1 High-resolution AFM images of the interface between mica and different experimental solutions. In each solution, both the topographic (purple–orange colour scale) and phase (blue colour scale) information are shown. (a) Hydration landscape of the mica surface in pure water. The lighter (higher) areas indicate regions where water molecules form an epitaxial lattice-like arrangement, with 2–3 nm wide domains. (b) In RbCl, the Rb^+ ions tend to form large correlated epitaxial domains, leading to an interface appearing almost uniform at this concentration. (c) K^+ ions behave in a similar fashion as Rb^+ (attractive correlation interactions at the interface), resulting in distinctive elongated domains (green arrow). (d) Na^+ ions exhibit no clear structural organization due to higher mobility and multiple solvation states. (e) Ca^{2+} ions also organise into domains but with many defects due to the multiple hydration states and adsorption to interstitial sites (position 2 in f). (f) Cartoon representation of the cleaved mica surface. The scale bar is 3 nm in all images. The colour scale represents height variations of 0.5 nm in topography and 30° in phase. All the ionic solutions with added salt (5 mM) are at pH 5.38. The temperature is 25.0 ± 0.1 °C.

measurements[64] with a shearing amplitude $A_t \sim 0.5$ nm, significantly smaller than mesoscale structures. A_t is also comparable to the smallest distance ions would diffuse when moving between adjacent lattice sites of the mica. Given the ion coverage of mica shown by the high resolution images, we expect, on average, at most one ion to be present between the confining tip and the mica surface, effectively conducting single ion-level nano-tribological measurements.

The results, presented in Fig. 2, confirm the lubricating effect of the added ions on the system where they reduce F_{shear} for a given applied force. The magnitude of the effect depends on the ion's charge density, following a standard Hofmeister series. The phase information shows that while the ions reduce F_{shear}, they increase the viscosity of the sheared liquid, with φ_t moving closer to 90° (Fig. 2b). This and the fact that E_{diss} also decreases when ions are added to the solution suggest that pure water adopts a glassy-like behaviour. Substantial friction between ordered hydration water layers increases the energy dissipated in the system following a mechanism analogous to boundary friction. Consistently, the system exhibits a significant elastic response in pure water. Adding ions ruptures this order and decreases the friction through an increase in local viscosity. In other words, the system appears to evolve towards a more liquid-like behaviour of the interface, better described by hydrodynamic friction. Both theoretical[65,66] and experimental studies[67,68] have shown

that water molecules on mica tend to acquire a crystalline, or ice-like arrangement in the first layer due to the approximate lattice matching between the mica surface and the hexagonal ice basal plane. When under nano-confinement, the diffusion of the water molecules decreases dramatically.[23,65]

Added ions frustrate the otherwise highly structured hydrogen bond network, limiting the range of intermolecular correlations and competing with the ordered mica surface for water molecules. This results in an increase in mobility for the water molecule in the nano-confined gap,[50,69] rendering the sheared solution more viscous. Ions with a larger charge density, ρ, exhibit a more cohesive hydration shell and tend to strongly restructure the water's hydrogen bond network,[70–72] leading to better lubrication properties. This is obvious from the difference in the friction coefficients derived for Rb^+ and Ca^{2+} (Fig. 2c). Na^+ exhibits a slightly anomalous behaviour that partly challenges this simple description due to its complex adsorption profile.[24,64,73,74] The contribution of anions can be neglected here given the important negative surface charge of both confining surfaces. Anions may gather in the upper hydration layers, but X-ray scattering and AFM show a rapid decrease of the degree of ordering in this region, indicating limited impact.[75,76]

The linear increase of F_{shear} with the confining force suggests that the system follows a simple hydrodynamic friction that can be characterised by a single, ion-dependent
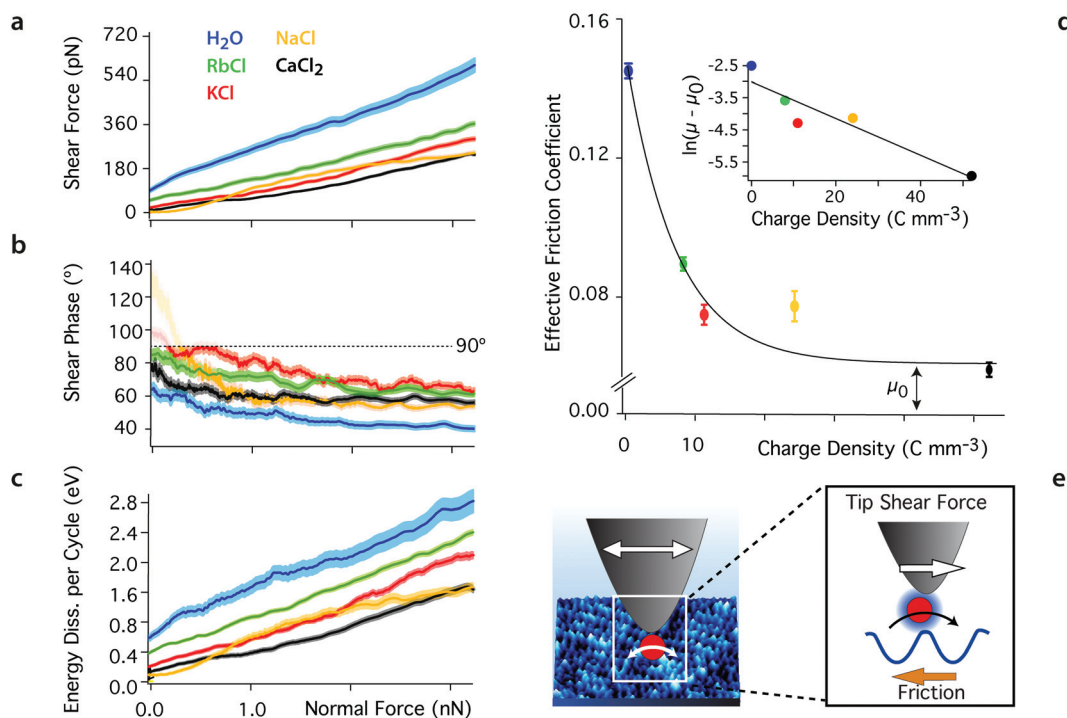
Fig. 2 Averaged shear force (a), shear phase (b) and energy dissipated per shear cycle (c) as functions of the confining force for the different aqueous solutions. The thickness of the curves represents the standard error. Added ions decrease the magnitude of the shear force F_{shear} at any given confining force by comparison with pure water, and the phase, φ_t, increases to values closer to 90°, indicating a more viscous behaviour of the sheared liquid. At low confining forces (<0.2 nN), the shear amplitude and hence force are close to the experimental noise level and the phase becomes undefined ($\varphi_t > 90°$, semi-transparent region). The energy dissipation, E_{diss}, also decreases with added ions, indicating less friction. The effective friction coefficient derived from (a) are shown in (d) with their standard error ($\mu_{water} = 0.142 \pm 0.002$, $\mu_{Rb} = 0.089 \pm 0.001$, $\mu_K = 0.074 \pm 0.003$, $\mu_{Na} = 0.077 \pm 0.004$, and $\mu_{Ca} = 0.059 \pm 0.002$). The magnitude of the coefficients decreases exponentially with the ion's charge density (inset in d) as expected from eqn (3) (see text). (e) The tip-driven shear motion of the ions at the surface of the mica lattice is captured by the Prandtl–Tomlinson model: the tip pulls ions between adjacent sites, over an energy barrier related to their hydration energy. All the solutions are at pH 5.38 and ionic solutions contain 5.0 mM salt. The temperature is 25 $\pm$ 0.1 °C.

coefficient. Empirically, we find an exponential relationship between the hydrodynamic friction coefficient and the charge density of the cations in the solution:

$$\mu = \mu_0 + \mu_H e^{-\lambda \rho}, \qquad (3)$$

where $\mu_0 = 0.061 \pm 0.002$ represents the minimal achievable friction coefficient, $\mu_H = 0.082 \pm 0.002$ is the maximum contribution to friction that depends on added ions, and $\lambda = 1.38 (\pm 0.09) \times 10^{-10} \text{ C}^{-1} \text{ m}^3$ is an empirical parameter. In this framework, μ_0 describes the friction in the absence of a cohesive hydrogen-bond network within the sheared layer, aside from the immediate hydration structure of mica. The amount of friction induced by reorganizing the cohesive hydrogen-bond network due to added ions is described by μ_H which has a magnitude comparable to μ_0. When under shear, ions move between adjacent adsorption sites (potential minima) by overcoming an energy barrier, E_a, related to the disruption of the hydrogen bond network and to their inter-action energy with the surface. The ions move through a thermally activated process,[23] here enhanced by the shearing tip that effectively 'pulls' ions to adjacent sites (Fig. 2e).

Conceptually, this interpretation is captured by the Prandtl–Tomlinson model[77,78] that describes the atomistic friction between a single atom and a periodic surface. Here, this translates as the tip being assimilated to a point mass that pulls single hydrated ions via an elastic spring over the periodic mica lattice. Because of the small amplitude used, ions are repeatedly dragged back and forth between adjacent sites of the lattice. While the Prandtl–Tomlinson model has become famous for its description of the atomistic stick-slip friction, its theoretical framework can also describe smooth sliding friction. This occurs when the energy barrier experienced by the atom moving between two adjacent lattice sites is significantly lower than the energy provided by the pulling spring:

$$\gamma = \frac{2\pi^2 U_0}{ka^2}, \qquad (4)$$

with γ the ratio between the energy barrier, U_0, and the spring pulling energy. The latter is characterised by the effective spring constant, k, and the lattice parameter, a. Smooth sliding is hence expected to occur when $\gamma \ll 1$.

In the present case, the energy barrier, E_a, experienced by hydrated ions moving between adjacent lattice sites of the

mica lattice can be deduced from the parameter λ in eqn (3). λ effectively captures the thermally-activated motion of the ions and must hence take the following form:

$$\lambda = \frac{E_a/q}{k_b T/a^3}, \qquad (5)$$

where E_a/q is the activation energy per unit charge q. The thermal energy (4.11×10^{-21} J or 25 meV at 25.0 °C) is taken per volume a^3 of the system, with a being a relevant length scale,[79] here half of mica's lattice parameter ($a = 0.26$ nm). We find $E_a \sim 1.26\, k_b T$ which corresponds to about half the energy needed to dehydrate the mica surface over an area of a^2. From eqn (4) and assuming $U_0 \sim E_a$, we find $\gamma \sim 10^{-3} \ll 1$, confirming the validity of our interpretation.

Overall, the model works remarkably well and provides a consistent interpretation of the molecular processes dominating the nano-shearing measurements. The applicability of the model also suggests a profound connection between the solid–solid boundary friction implicitly assumed by the Prandtl–Tomlinson model and the hydrodynamic friction observed here for ions at interfaces: at the nanoscale, hydrodynamic friction can be understood as an extreme case of boundary friction where ions and molecules are pulled across the interface in a low γ regime that enables smooth motion. In this framework, the friction force can then be understood in terms of local solvation effects and disruption of the hydrogen bond network that oppose the motion of the molecule considered at the interface, similarly to U_0 in the Prandtl–Tomlinson model.

From a purely thermodynamics perspective, the same process can be explained by the reduced entropy of the confined system whereby the imposed shear force precludes ions from moving randomly at the interfaces and freely probe all the available configurational states. This explains the fact that, for a given applied force, a decrease in the charge density of the added ion increases F_{shear} and E_{diss}: ions with lower ρ exhibit a weaker solvation shell that can be easily disrupted by the confining tip. More work is hence needed to compensate for the associated tip-induced entropy reduction.

The ionic sequence found here for the effective friction coefficients contrasts with SFB findings.[31] This discrepancy could suggest that the two techniques probe different physical phenomena, due to the different sizes in the nano-confined areas they explore. The mesoscale order visible for K$^+$ ions in Fig. 1 is likely to influence SFB measurements, for example inducing local jamming and overlap during the lateral motion of ions and water molecules within the confined layer. Additionally, the ionic concentration probed here is relatively low, to ensure single ion level measurements. At higher concentrations, the confined hydrogen bond network becomes saturated with ions and other effects can take place such as ion-ion friction or the sliding past of dense Stern layers. To explore these effects, we quantified the dependence of F_{shear}, φ_t and E_{diss} on KCl concentration (Fig. 3). At low ionic concentration (<75 mM KCl), the adjunction of ions enhances the lubricating properties of the confined solution, but the solu-
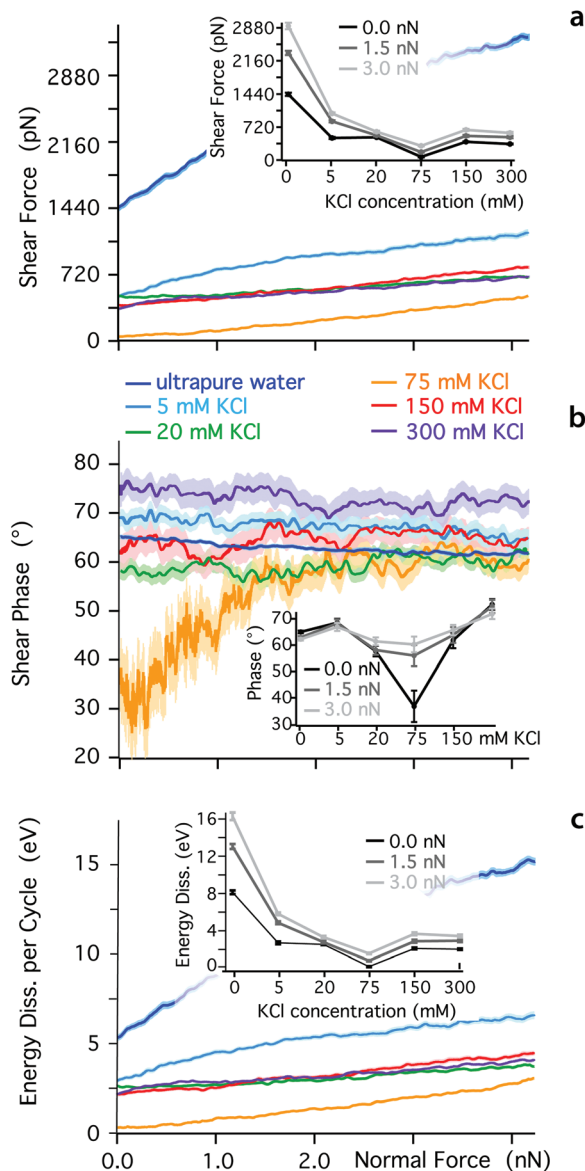

Fig. 3 Evolution of the shear force (a), phase (b) and energy dissipated per shear cycle (c) as functions of the confining force for different concentrations of KCl in aqueous solutions. The evolution is non-monotonous with a minimum in F_{shear} and E_{diss} at 75 mM KCl, coinciding with a strongly elastic behaviour of the confined liquid. This is clearly visible at low confining pressures (~0 nN). For easier comparison, the insets (a–c) show respectively F_{shear}, φ_t and E_{diss} as functions of ionic concentration for given applied forces.

tion becomes progressively more elastic under a given applied load already past 5 mM KCl (inset Fig. 3b). Around 75 mM KCl, the system reaches minimum of friction, but through an almost completely elastic behaviour. This could be interpreted as 'dry' boundary friction with the K$^+$ ions arranged in such a manner that the confined hydrogen bond network plays a minimal role. At such high concentration, the mica is saturated with cations[23,80] and multiple layers of ions may exist between the tip and the surface. Past 75 mM KCl, the lubrica-

tion properties of the solution deteriorate, and the response under shear becomes again more viscous. The ionic concentration corresponding to the friction minimum is only approximately identified but the results clearly indicate a non-monotonic behaviour, also confirming previous studies in NaCl.[81] Qualitatively, this non-monotonicity should be expected since ions can no longer behave as dissolved 'point perturbations' to the hydrogen bond network past a certain concentration, but rather become the dominating feature with its own characteristics. Overall, these results highlight the importance of both spatial and temporal scales as well as ionic concentration when characterising the behaviour of confined fluids.

Shear-spectroscopy: soft confinement

The impact of the cations on the behaviour of the nano-confined water's hydrogen bond network can also be observed further away from the mica surface, with several layers of water and ions between the tip and the surface. This is done by examining changes in F_{shear}, φ_t and E_{diss} as functions of the tip–sample distance. The results of this experiment are shown in Fig. 4. In pure water, F_{shear} increases already when the tip is still ~2 nm away from the mica surface. In contrast, F_{shear} increases only at distances smaller than ~0.5 nm when salt is added to the solution. No clear trend links ρ and F_{shear} or E_{diss} except for an increase in the effective viscosity, consistent with better-ordered interfacial water layers. The effective viscosity η_{eff} of the nano-confined liquid under shear can be quantified as follows:[29]

$$\eta(d) = \frac{F_{shear}(d+b)}{Av},\qquad(6)$$

where A is the tip–sample contact area, η_{bulk} the bulk solution viscosity at 25 °C (890 μPa s),[82] b the slip length of the liquid at the interface with mica, and v the shearing velocity. Here, the average shearing velocity is v = 550 m s^{-1} and b = 0 (no-slip).[29] The significant increase in η_{eff} for ultrapure water supports the hypothesised glassy-like behaviour under nano-confinement (Fig. 2b) and agrees with previous AFM studies in similar conditions.[83]

Eqn (6) implicitly assumes a continuous fluid, a hypothesis that tends to break down at very short tip–sample distances where the molecular nature of water can no longer be ignored.[17] In pure water, this breakdown is observed for nano-confinement distances smaller than about two water molecules (dotted vertical blue line in Fig. 4b), characterised by a subsequent decrease of η_{eff}. Interestingly, a second step-like decrease of η_{eff} can be seen at a distance of ~0.25 nm (dotted yellow line), the approximate thickness of a single water layer. These observations suggest that the apparent decrease of η_{eff} can be explained by the tip disrupting ordered, solid-like confined water layers. This is consistent with the significant elastic response of pure water, its glassy-like behaviour and the existence of long-range order in the hydrogen bond network.

The presence of ions dramatically reduces η_{eff} that decreases only for nano-gaps thinner than a single water layer. This highlights the fact that the ions' lubricating properties
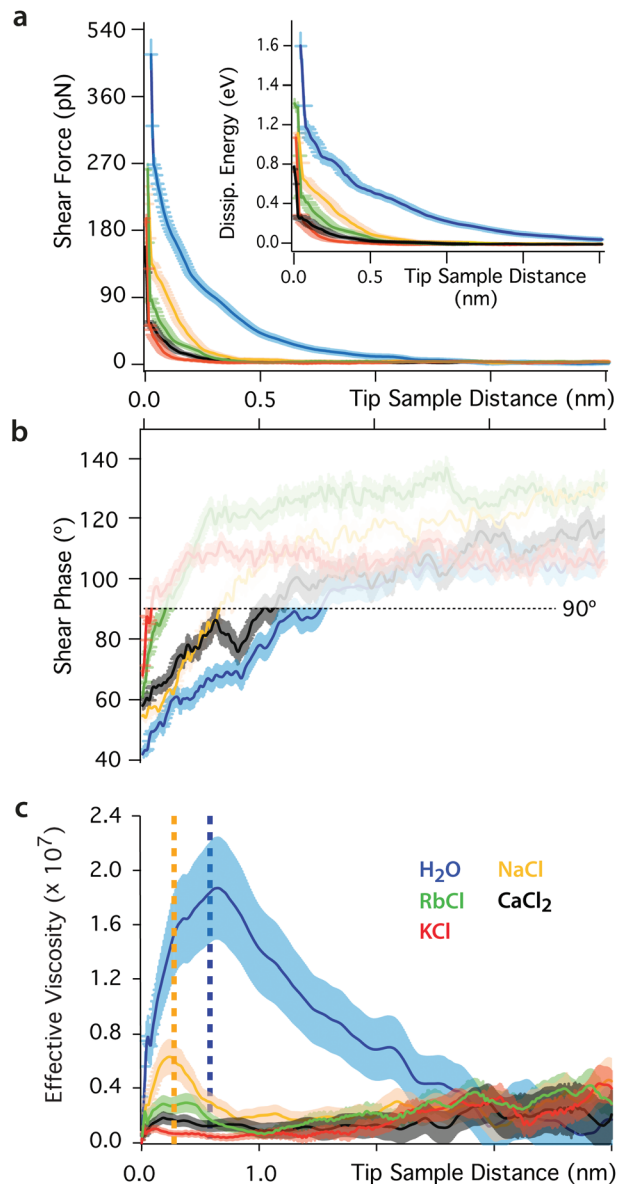

Fig. 4 Shear force (a), phase (b) and effective viscosity (c) as functions of the tip−sample distance. The force increases below distances of ~2 nm in pure water and ~0.5 nm in ionic solution. The inset in (a) shows the evolution of the energy dissipated per shear cycle. The response of nano-confined water induces a greater dissipation of energy than in ionic solutions. In (b) the phase is undefined at large tip−sample distance due to the shear amplitude and force being close to the noise level (φ_t > 90°, semi-transparent region). (c) The effective viscosity of the interfacial liquid increases by orders of magnitude in pure water, but changes in ionic solutions are close to the noise limit (except for NaCl). The yellow and blue dotted lines indicate regions where the confinement is smaller than one or two water molecules, respectively. For such small nanogaps, the assumption of continuous fluid implicit to eqn (6) breaks down.[17] In the non-contact region, the shearing area is $A \sim 10$ nm^2. The slip length of mica was taken to be zero.[29]

originate from their ability to disrupt the ordered molecular arrangement of nano-confined water molecules, thereby inducing a greater fluidity of the liquid.[50,69,70–72]

Aside from calculating η_{eff}, it is also possible to derive the storage, G', and loss, G'', moduli of the confined liquid (ESI, Fig. S5†) and obtain an estimate of the system's relaxation time τ:[17]

$$\tau = \frac{G'}{G''\omega}, \tag{7}$$

τ describes the time needed for liquid molecules to relax, overcome the local solid-like order and reach the configuration of minimum free energy. Here, we find $\tau \sim 0.01$ ms–0.1 ms, several orders of magnitude slower than for bulk water, but slightly faster than the 60 ms dielectric relaxation time of supercooled water between 170 K and 210 K.[17] Similarly to supercooled water, the dynamics of a glass-forming liquid is governed by the collective motions of the molecules over the cooperative length.[36] In this framework, the relaxation timescale is related to reorientation dynamics of the confined water molecules when forming hydrogen bonds, preferentially parallel and perpendicular to the shearing direction.[23] This is in stark contrast with bulk water where no global preferred arrangements of dipole exists.[37] Adding cations helps break the global symmetry of the confined system, leading to a faster relaxation.[31] We note that τ must be understood as an order of magnitude since it was not possible to explore different oscillation frequencies, ω.

The effect of pH

One key aspect of measurements involving nano-confined water is the solution's pH. The hydronium ions compete with dissolved metal cations[23,80,84] and the dipole of the water molecules[23] for neutralising mica's negative surface charge. As a result, changes in pH can have a dramatic effect on the molecular organisation and dynamics of interfacial water, often with consequences on the interface's tribological properties. At low pH, most of mica's surface charge is neutralised by strongly bound hydronium ions[84] and metal ions tend to remain dissolved in the bulk solution due to their comparatively lower affinity for the mica surface.[84] To test this interpretation, we conducted shear experiments at three different pH for each of the ionic solutions investigated. Representative results for the KCl solution are presented in Fig. 5. Results in the other solutions exhibit a similar trend and are hence presented in ESI for clarity (Fig. S6–S9†). As the pH decreases, both F_{shear} and E_{diss}, increase (Fig. 5a), confirming the replacement of metal cations by hydronium ions. Hydronium ions limit the cations' ability to disrupt the ordered hydrogen bond network, but have a smaller impact on pure water (see ESI, Fig. S6†) given the similar hydration structures of H_3O^+ and pure water.[35] Dissolved ions can alter the interfacial network, but this is dependent on the charge density of the confining surface itself, which is controlled by the pH.
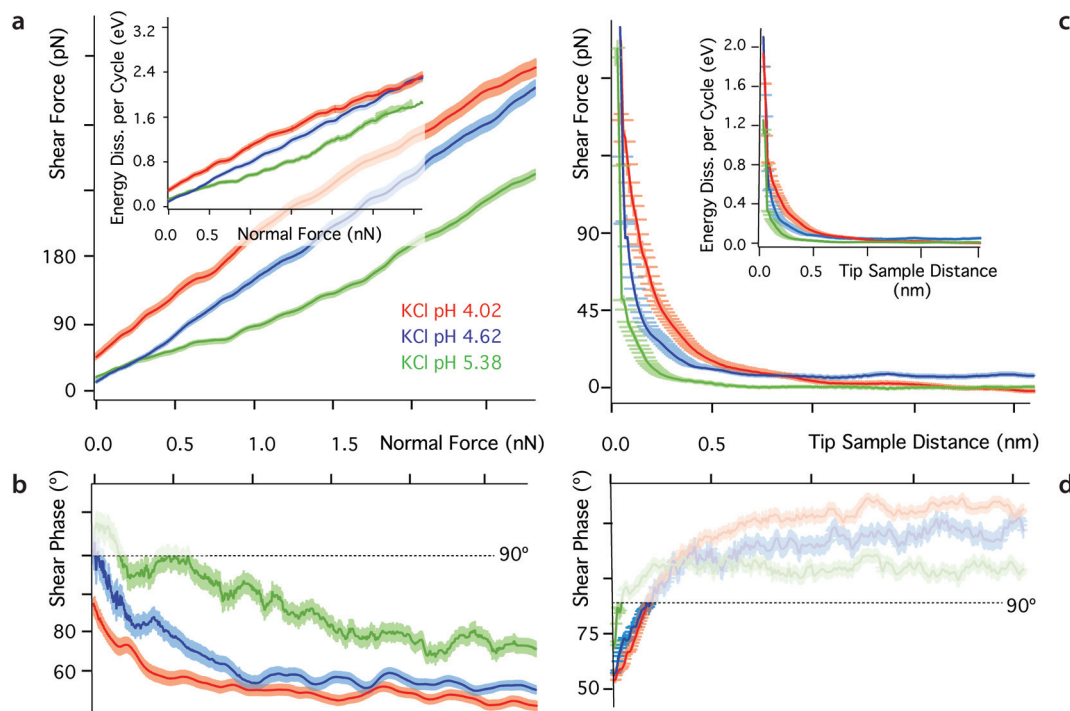

Fig. 5 Evolution of the shear force, energy dissipated per shear cycle and phase as functions of pH in KCl. Results are shown for hard confinement (a–b) and soft confinement (c–d). The insets in (a) and (c) show the energy dissipated per shear cycle. At tip–sample distance < 0.5 nm, the shear force and the energy dissipation increase with decreasing pH. These results are consistent with hydronium ions competing with metal cations for binding sites on mica, thereby limiting the metal cations' ability to lubricate the system. The experiments are performed at 25 ± 0.1 °C. In (b) and (d) the phase is undefined at large tip–sample distance and small confining forces due to the shear amplitude and hence force being close to the noise level ($\varphi_t > 90°$, semi-transparent region).

Conclusions

This study combines atomic-level resolution AFM imaging with sub-nanometre shear-force spectroscopy to examine the nano-tribological properties of aqueous solutions under shear down to the single ion level. Results obtained in five different aqueous solutions (ultrapure water, RbCl, KCl, NaCl, and CaCl$_2$) and at different pH show that the behaviour of nano-confined water can be quantitatively interpreted in terms of the restructuring dynamics of its hydrogen bond network. Under strong confinement, the system is dominated by the thermally activated motion of ions between adjacent sites of the confining mica surface, with an energy barrier determined by the mica and the ions' hydration structures. The ions disrupt the otherwise ordered hydrogen bond network of the liquid and act as lubricants, whose effectiveness follows a direct Hofmeister series. Under softer confinement, the ions still disrupt water's hydrogen bond network, but ion-specificity is no longer obvious. Lowering the pH of the solution tends to replace adsorbed metal ions by hydronium, thereby rendering the system more elastic and increasing the measured friction. High-resolution imaging reveals some mesoscopic ordering of ions within the Stern layer, suggesting that the nanoscale shear force measurements conducted here cannot be extrapolated directly from measurements involving larger confining areas and shear amplitudes. Further studies are needed to investigate the effect of the shearing velocity and extend the current findings to other ionic species, including for potential technological applications in the fields of energy and the design of the 'ultimate green' water-based lubricants.[12]

Conflicts of interest

There are no conflicts to declare.

Acknowledgements

References

1 O. Björneholm, M. H. Hansen, A. Hodgson, L.-M. Liu, D. T. Limmer, A. Michaelides, P. Pedevilla, J. Rossmeisl, H. Shen, G. Tocci, E. Tyrode, M.-M. Walz, J. Werner and H. Bluhm, *Chem. Rev.*, 2016, **116**, 7698–7726.

2 T. D. Li, J. Gao, R. Szoszkiewicz, U. Landman and E. Riedo, *Phys. Rev. B*, 2007, **75**, 115415.

3 M. N. Levy, R. M. Berne, B. M. Koeppen and B. A. Stanton, *Berne & Levy principles of physiology*, Mosby, 2006.

4 P. M. Wiggins, *Microbiol. Rev.*, 1990, **54**, 432–449.

5 R. Milke, R. Dohmen, H. W. Becker and R. Wirth, *Contrib. Mineral. Petrol.*, 2007, **154**, 519–533.

6 M. Ricci, P. Spijker, F. Stellacci, J.-F. Molinari and K. Voïtchovsky, *Langmuir*, 2013, **29**, 2207–2216.

7 S. Granick, S. Bae, S. Kumar and C. Yu, *Physics*, 2010, **3**, 18–21.

8 R. J. Mashl, S. Joseph, N. R. Aluru and E. Jakobsson, *Nano Lett.*, 2003, **3**, 589–592.

9 F. Ridi, E. Fratini and P. Baglioni, *J. Colloid Interface Sci.*, 2011, **357**, 255–264.

10 H. E. Stanley, S. V. Buldyrev, G. Franzese, P. Kumar, F. Mallamace, M. G. Mazza, K. Stokely and L. Xu, *J. Phys.: Condens. Matter*, 2010, **22**, 284101.

11 D. Bradshaw, A. Garai and J. Huo, *Chem. Soc. Rev.*, 2012, **41**, 2344–2381.

12 S. Liu, D. Guo and G. Xie, *J. Appl. Phys.*, 2010, **108**, 084315.

13 N. Giovambattista, P. J. Rossky and P. G. Debenedetti, *Phys. Rev. Lett.*, 2009, **102**, 050603.

14 E. Tombari, G. Salvetti, C. Ferrari and G. P. Johari, *J. Chem. Phys.*, 2005, **122**, 104712.

15 R. Zangi, *J. Phys.: Condens. Matter*, 2004, **16**, S5371–S5388.

16 T. Mitsui, M. K. Rose, E. Fomin, D. F. Ogletree and M. Salmeron, *Science*, 2002, **297**, 1850–1852.

17 T. D. Li and E. Riedo, *Phys. Rev. Lett.*, 2008, **100**, 106102.

18 M. J. Dellostritto, J. D. Kubicki and J. O. Sofo, *Langmuir*, 2016, **32**, 11353–11365.

19 N. Giovambattista, P. J. Rossky and P. G. Debenedetti, *Phys. Chem.*, 2012, **63**, 179–200.

20 S. Smirnov, I. Vlassiouk, P. Takmakov and F. Rios, *ACS Nano*, 2010, **4**, 5069–5075.

21 L. Liu, S.-H. Chen, A. Faraone, C.-W. Yen and C.-Y. Mou, *Phys. Rev. Lett.*, 2005, **95**, 117802.

22 W. H. Briscoe, S. Titmuss, F. Tiberg, R. K. Thomas, D. J. McGillivray and J. Klein, *Nature*, 2006, **444**, 191–194.

23 M. Ricci, W. Trewby, C. Cafolla and K. Voïtchovsky, *Sci. Rep.*, 2017, **7**, 43234.

24 M. Ricci, P. Spijker and K. Voïtchovsky, *Nat. Commun.*, 2014, **5**, 4400.

25 K. Voitchovsky and M. Ricci, *Proc. SPIE*, 2012, **8232**, 82320O.

26 M. A. Ricci, V. Tudisca, F. Bruni, R. Mancinelli, E. Scoppola, R. Angelini, B. Ruzicka and A. K. Soper, *J. Non-Cryst. Solids*, 2015, **407**, 418–422.

27 D. Argyris, D. R. Cole and A. Striolo, *ACS Nano*, 2010, **4**, 2035–2042.

28 U. Raviv, S. Perking, P. Laurat and J. Klein, *Langmuir*, 2004, **20**, 5322–5332.

29 D. Ortiz-Young, H.-C. Chiu, S. Kim, K. Voïtchovsky and E. Riedo, *Nat. Commun.*, 2013, **4**, 2482.

30 A. Malani and K. G. Ayappa, *J. Chem. Phys.*, 2012, **136**, 194701.

31 A. Gaisinskaya-Kipnis, L. Ma, N. Kampf and J. Klein, *Langmuir*, 2016, **32**, 4755–4764.

32 A. Ulcinas, G. Valdre, V. Snitka, M. J. Miles, P. M. Claesson and M. Antognozzi, *Langmuir*, 2011, **27**, 10351–10355.

33 G. Zhao, Q. Tan, L. Xiang, D. Cai, H. Zeng, H. Yi, Z. Ni and Y. Chen, *J. Chem. Phys.*, 2015, **143**, 104705.

34 I. Waluyo, C. Huang, D. Nordlund, U. Bergmann, T. M. Weiss, L. G. M. Pettersson and A. Nilsson, *J. Chem. Phys.*, 2011, **134**, 064513.

35 L. Cheng, P. Fenter, K. L. Nagy, M. L. Schlegel and N. C. Sturchio, *Phys. Rev. Lett.*, 2001, **87**, 156103.

36 S. Cerveny, J. Colmenero and A. Alegría, *Eur. Phys. J.*, 2007, **141**, 49–52.

37 W. Qi, J. Chen, J. Yang, X. Lei, B. Song and H. Fang, *J. Phys. Chem. B*, 2013, **117**, 7967–7971.

38 H. Sakuma, K. Otsuki and K. Kurihara, *Phys. Rev. Lett.*, 2006, **96**, 046104.

39 S. Perkin, R. Goldberg, L. Chai, N. Kampf and J. Klein, *Faraday Discuss.*, 2009, **141**, 399–413.

40 C. D. Dushkin and K. Kurihara, *Colloids Surf., A*, 1997, **129**, 131–139.

41 H. Kawai, H. Sakuma, M. Mizukami, T. Abe, Y. Fukao, H. Tajima and K. Kurihara, *Rev. Sci. Instrum.*, 2008, **79**, 043701.

42 U. Raviv and J. Klein, *Science*, 2002, **297**, 1540–1543.

43 S. H. Khan, G. Matei, S. Patil and P. M. Hoffmann, *Phys. Rev. Lett.*, 2010, **105**, 106101.

44 T. Fukuma, K. Kobayashi, K. Matsushige and H. Yamada, *Appl. Phys. Lett.*, 2005, **87**, 034101.

45 D. Naumenko, V. Snitka, E. Serviene, I. Bruzaite and B. Snopok, *Analyst*, 2013, **138**, 5371–5383.

46 A. Shiotari and Y. Sugimoto, *Nat. Commun.*, 2017, **8**, 14313.

47 E. J. Miller, W. Trewby, A. Farokh Payam, L. Piantanida, C. Cafolla and K. Voïtchovsky, *J. Visualized Exp.*, 2016, **118**, e54924.

48 J. Klein, U. Raviv, S. Perkin, N. Kampf, L. Chai and S. Giasson, *J. Phys.: Condens. Matter*, 2004, **16**, S5437–S5448.

49 J. Klein, *Friction*, 2013, **1**, 1–23.

50 A. Gaisinskaya, L. Ma, G. Silbert, R. Sorkin, O. Tairy, R. Goldberg, N. Kampf and J. Klein, *Faraday Discuss.*, 2012, **156**, 217–233.

51 Y. Leng and P. T. Cummings, *Phys. Rev. Lett.*, 2005, **94**, 026101.

52 A. Malani, K. G. Ayappa and S. Murad, *J. Phys. Chem. B*, 2009, **113**, 13825–13839.

53 S. S. Lee, P. Fenter, K. L. Nagy and N. C. Sturchio, *Nat. Commun.*, 2017, **8**, 15826.

54 I. Siretanu, D. Ebeling, M. P. Andersson, S. L. S. Stipp, A. Philipse, M. C. Stuart, D. van den Ende and F. Mugele, *Sci. Rep.*, 2015, **4**, 4956.

55 F. H. J. Van Der Heyden, D. J. Bonthuis, D. Stein, C. Meyer and C. Dekker, *Nano Lett.*, 2007, **7**, 1022–1025.

56 W. Trewby, D. Livesey and K. Voïtchovsky, *Soft Matter*, 2016, **12**, 2642–2651.

57 L. Piantanida, H. L. Bolt, N. Rozatian, S. L. Cobb and K. Votchovsky, *Biophys. J.*, 2017, **113**, 426–439.

58 H.-J. Butt and M. Jaschke, *Nanotechnology*, 1995, **6**, 1–7.

59 N. Mullin and J. K. Hobbs, *Rev. Sci. Instrum.*, 2014, **85**, 113703.

60 K. Voitchovsky, J. J. Kuna, S. A. Contera, E. Tosatti and F. Stellacci, *Nat. Nanotechnol.*, 2010, **5**, 401–405.

61 M. Urbakh, J. Klafter, D. Gourdon and J. Israelachvili, *Nature*, 2004, **430**, 525–528.

62 T. Fukuma, Y. Ueda, S. Yoshioka and H. Asakawa, *Phys. Rev. Lett.*, 2010, **104**, 016101.

63 K. Voïtchovsky, *Nanoscale*, 2016, **8**, 17472–17482.

64 K. Kobayashi, Y. Liang, S. Murata, T. Matsuoka, S. Takahashi, N. Nishi and T. Sakka, *Langmuir*, 2017, **33**, 3892–3899.

65 Y. Leng and P. T. Cummings, *J. Chem. Phys.*, 2006, **124**, 074711.

66 M. Odelius, M. Bernasconi and M. Parrinello, *Phys. Rev. Lett.*, 1997, **78**, 2855.

67 A. Verdaguer, G. M. Sacha, H. Bluhm and M. Salmeron, *Chem. Rev.*, 2006, **106**, 1478–1510.

68 P. B. Miranda, L. Xu, Y. R. Shen and M. Salmeron, *Phys. Rev. Lett.*, 1998, **81**, 5876.

69 J. S. Kim and A. Yethiraj, *J. Phys. Chem. B*, 2008, **112**, 1729–1735.

70 B. Hribar, N. T. Southall, V. Vlachy and K. A. Dill, *J. Am. Chem. Soc.*, 2002, **124**, 12302–12311.

71 I. A. Topol, G. J. Tawa, S. K. Burt, S. K. Burt and A. A. Rashin, *J. Chem. Phys.*, 1999, **111**, 10998–11014.

72 J. E. Combariza and N. R. Kestner, *J. Phys. Chem.*, 1995, **99**, 2717–2723.

73 S. S. Lee, P. Fenter, K. L. Nagy and N. C. Sturchio, *Langmuir*, 2012, **28**, 8637–8650.

74 H. Sakuma and K. Kawamura, *Geochim. Cosmochim. Acta*, 2011, **75**, 63–81.

75 S. Pintea, W. De Poel, A. E. F. De Jong, V. Vonk, P. Van Der Asdonk, J. Drnec, O. Balmes, H. Isern, T. Dufrane, R. Felici and E. Vlieg, *Langmuir*, 2016, **32**, 12955–12965.

76 K. Kimura, S. Ido, N. Oyabu, K. Kobayashi, Y. Hirata, T. Imai and H. Yamada, *J. Chem. Phys.*, 2010, **132**, 194705.

77 E. Gnecco, R. Bennewitz, T. Gyalog and E. Meyer, *J. Phys.: Condens. Matter*, 2001, **13**, 619–642.

78 R. Guerra, A. Vanossi and M. Urbakh, *Phys. Rev. E*, 2010, **78**, 03611.

79 A. Erbaş, D. Horinek and R. R. Netz, *J. Am. Chem. Soc.*, 2011, **134**, 623–630.

80 C. Park, P. A. Fenter, K. L. Nagy and N. C. Sturchio, *Phys. Rev. Lett.*, 2006, **97**, 016101.

81 S. H. Khan, E. L. Kramkowski and P. M. Hoffmann, *Langmuir*, 2016, **32**, 10802–10807.

82 J. Kestin, M. Sokolov and W. A. Wakeham, *J. Phys. Chem. Ref. Data*, 1978, **71**, 941–948.

83 T. D. Li, H. C. Chiu, D. Ortiz-Young and E. Riedo, *Rev. Sci. Instrum.*, 2014, **85**, 123707.

84 C. Park, P. A. Fenter, N. C. Sturchio and K. L. Nagy, *Langmuir*, 2008, **24**, 13993–14004.